Terrestrial Planet Finder Coronagraph Pointing Control System Design and Evaluation for Flight Baseline 1

Kuo-Chia Liu[a], Carl Blaurock[b], James Alexander[c], Larry Dewell[d]
[a]NASA Goddard Space Flight Center, 8800 Greenbelt Road, Greenbelt, MD 20771
[a]Nightsky Systems, Inc. 3916 Lauriston Rd., Raleigh NC 27616
[c]NASA Jet Propulsion Laboratory, Palo Alto, CA 91109
[d]Lockheed Martin Advanced Technology Center, Palo Alto, CA 94304

ABSTRACT

The Terrestrial Planet Finder mission will search for Earth-like, extrasolar planets. The Coronagraph architecture option (TPF-C) will use contrast imaging to suppress the bright starlight in order to detect reflected visible light from the planet. To achieve the required contrast ratio stability of 2e-11, the payload pointing stability must be maintained to better than 4 milli-asec (1σ). The passive TPF-C pointing architecture uses a 3-stage control system combined with a 2-stage passive isolation system to achieve the required pointing accuracy. The active pointing stage includes reaction wheels used for coarse pointing of the spacecraft, a position controlled secondary mirror that provides intermediate alignment, and a Fine Guidance Mirror that provides fine steering control.

Each stage of the Pointing Control System (PCS) introduces some pointing inaccuracy due to actuator non-idealities that cause the physical commands to deviate by some amount from the ideal command, by sensor noises that are fed back through that stage's actuators to produce physical motions, and by modeling errors that arise because of imprecise knowledge of the dynamics of the system. The PCS must demonstrate the required accuracy of pointing performance in the presence of all of these effects. This paper presents the baseline PCS design and preliminary performance results. These results are compared to the TPF-C error requirements in order to assess the viability of the flight baseline design.

Keywords: Pointing control, control architecture, dynamic simulation, slew performance

1.0 INTRODUCTION

The Terrestrial Planent Finder Coronagraph (TPF-C) is one of the current concepts for detecting and characterizing extrasolar planets orbiting nearby stars. The coronagraph instrument is a space-based observatory with 8 m by 3.5 m primary mirror that aims to reject the starlight and detect the reflected planet light in the visible range. A deployed configuration of TPF-C is shown in Figure 1. Dynamic jitter, introduced by environmental and on-board mechanical disturbances, degrades the optical performance (image quality) and the capability to reject starlight (contrast ratio). The TPF coronagraph must maintain the dynamic stability of its instrument to the sub-milliasec (mas) and nanometer (nm) level in order to successfully perform contrast imaging required for planet detection. Meeting these stringent stability requirements in the presence of dynamic jitter imposes significant technical challenge on the pointing and vibration isolation systems.

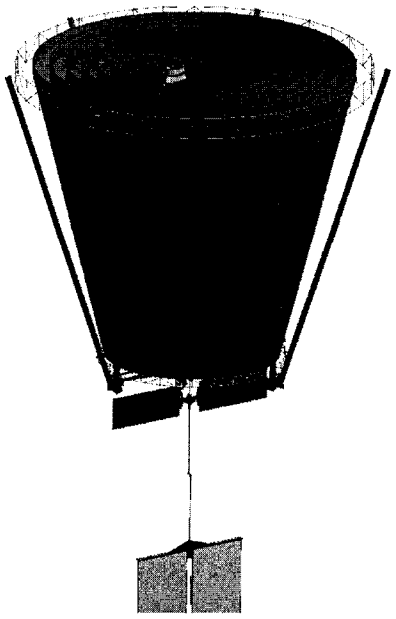

Figure 1 Deployed configuration of TPF-C (figure by Tim Ho)

For the flight baseline 1 (FB1) design[1], the pointing control system team has developed two vibration isolation schemes: passive and active. Both of the isolation approaches have been thoroughly evaluated during the FB1 analysis cycle, and their performance results can be found in two companion papers[2,3]. The objective of this paper is to provide a detailed overview of the pointing control architecture created for FB1. It focuses on the design and analysis of the pointing system with the passive isolation option, whereas the active pointing architecture and analysis will be the subject of a different paper. To evaluate the

performance of the current design, a time-domain simulation has been developed to incorporate spacecraft dynamics, actuator and sensor models, control algorithms, and optical performance models. The simulation results demonstrate the pointing stability for various control modes and assess the time required to perform large slew/settle maneuvers.

This paper first provides an overview of the pointing control system (PCS), discusses important dynamic requirements, and describes the current acquisition strategy in Section 2. Brief descriptions of common pointing actuator and sensor hardware employed for FB1, along with more detailed discussions on guiding system designs are given in Section 3. From the acquisition scenario, three pointing modes including coarse, acquisition, and fine pointing have been developed. Each of the three pointing modes and the corresponding control algorithms are discussed in Section 4. Performance simulations that illustrate some of the nonlinear actuator effects and slew/settle performance are shown in Section 5. A summary of the current analysis and direction for future work are outlined in Section 6.

2.0 POINTING CONTROL SYSTEM OVERVIEW

The TPF-C pointing control system uses several control loops, combined with vibration isolation, to meet the requisite dynamic stability requirements. There are four possible control systems that operate during observation: (1) spacecraft attitude control system (ACS), (2) fine stage payload pointing, (3) secondary mirror control (SMC), and (4) image motion control (IMC). The PCS team is currently considering both passive and active vibration isolation approaches.

2.1 Passive and active isolation systems

The passive isolation system features a two-stage isolation design. The first stage isolates the reaction wheel assembly, one of the major disturbance sources, from the spacecraft support module, while the second stage isolates the payload from the spacecraft. The corner frequencies of the reaction wheel assembly and the spacecraft-payload isolation stages are targeted at 1.5 and 1 Hz, respectively. This design uses flight-proven mechanical components (flexures and damping mechanisms) and does not require additional actuators/sensors operating during observation. However, the performance of the passive isolator is limited at low frequencies by the isolator corner frequency and at high frequency by the isolation floor. Detailed modeling of the passive system and its linear performance results are detailed in ref. 2.

The active isolation system is based on the disturbance free payload (DFP) design developed at the Lockheed Martin Advanced Technology Center. The DPF technology achieves isolation through nearly complete separation between the payload and spacecraft support module, and uses interface sensors and actuators to provide inertial pointing and maintain proximate separation of the bodies. This approach greatly reduces the disturbances transmitted through the spacecraft-payload interface while providing a more accurate pointing stage of the payload. The performance limitation of the DFP depends on the stiffness of the cable bundle that connects across the spacecraft-payload interface and back-EMF coupling that occurs through the non-contact actuators. More detailed descriptions of the DFP and its disturbance rejection performances can be found in a separate paper[3].

Although the DFP can potentially provide greater isolation capability than the passive isolation design, it is a relatively new technology with no flight heritage. The PCS team plans to carry both passive and active isolation systems through various design iterations and thoroughly understand the cost and risks related to each system before down-selecting an isolation system for TPF-C. The pointing control architecture described in this paper focuses on the passive isolation option and will include the DFP system in future work.

2.2 Requirements

The PCS design for FB1 aims to satisfy the dynamic requirements specified in the current error budget[4]. The error budget has top level contrast stability requirements with contributors from dynamically induced errors:

1. Beam walk - motion of beam across each optical element. Payload rigid body pointing errors or movements of optics can cause beam to shift location along optical surfaces.
2. Image motion – jitter causes light distribution that leaks around the mask to vary and degrades planet detectability.
3. Aberrations - wavefront errors arise from the optical system perturbed from its nominal configuration. Errors can result from optics moving relative to each other (structural deformation (SD)) or from bending of optics. For FB1 analysis, only the primary mirror (PM) can deform its shape and introduce aberration errors.
4. Mask error - Non-idealities of the mask transmission performance. Mask errors can be introduced by manufacturing errors, polarization effects, or wavelength dependence of mask materials[4].

The contrast error budget due to dynamic errors has seven contributors, resulting from combinations of the above errors:

Beam Walk	LOS	LOS mask error	Structure Deformation	SD mask error	PM deformation	PM def. mask error	**Total (sum)**
1.90E-12	9.04E-14	5.46E-13	2.75E-17	1.64E-17	8.55E-13	5.19E-15	**3.40E-12**

The current error budget is based on an 8th-order, band-limited mask. Analysis has shown that the contrast performance when employing this mask is limited by shearing of the starlight beam across imperfect optics (or beam walk)[4]. This constraint in turn places stringent requirements on rigid body pointing (4 mas 1σ), LOS jitter (0.3 mas 1σ), and relative position between secondary mirror (SM) and the PM (sub-micron level). Although the capability to convert pointing and optic motion errors to contrast exists, this paper uses only pointing-related metrics (i.e. rigid body pointing and LOS) to evaluate the performance of the PCS design.

2.3 Acquisition Scenario

This section provides a brief discussion of the nominal target acquisition, the process to place a designated star on the coronagraph mask, and the observation process as currently envisioned. The important parameters to be considered are the size of the coronagraph mask (approximately 60 mas across) and the image motion requirement (<0.3 asec) at the mask. Nominal target acquisition and observation proceed in three phases of pointing differing primarily in the particular sensor and level of pointing accuracy at each phase. Figure 2 shows the relative field of view (FOV) sizes, and the accuracy required during the modes.

1. Coarse pointing and slew - In this phase, telescope pointing is commanded by the spacecraft which relies on the S/C star trackers (~15 (3σ) asec in the two cross boresight axes, 60 (3σ) asec around the boresight), and gyros. While the noise equivalent angle (NEA) of the star tracker is ~ 5 asec, the angle random walk of the gyros is low enough to give pointing stability of better than 1 asec when combined with the star tracker signal. The coarse pointing control allows the telescope to be slewed to a specific inertial attitude.
2. Acquisition - Two payload star acquisition cameras (PSACs) are needed to bridge the gap between the pointing accuracy of the star tracker system and the FOV of the fine guidance sensor (FGS). At the completion of the slew, the attitude knowledge is better than 60 asec (worst axis). The stars falling within the PSAC FOV are then also known to better than 60 asec, and can be easily identified with simple star identification algorithms. After identification in the two PSAC camera FOV, the attitude of the payload can be recomputed to provide better than 100 mas (200 mas roll), 1σ. Using this refinement of attitude, the Payload can then be re-pointed to place the coronagraph star within the 3 asec diameter FGS FOV detector.
3. Fine (coronagraph) pointing – The FGS and coronagraph detector signals are used to move the target star to the center of the 60-mas-wide mask. The SM and spacecraft rigid body pointing are used as the pointing actuators, in preference to the fine guidance mirror (FGM), since this minimizes beam walk on the optics. The FGM is then used to scan the target star across the mask, to determine the location that achieves the minimum signal leakage past the coronagraphic mask. The corresponding star location as measured by the FGS is used as the reference position for the image motion control system during observation.

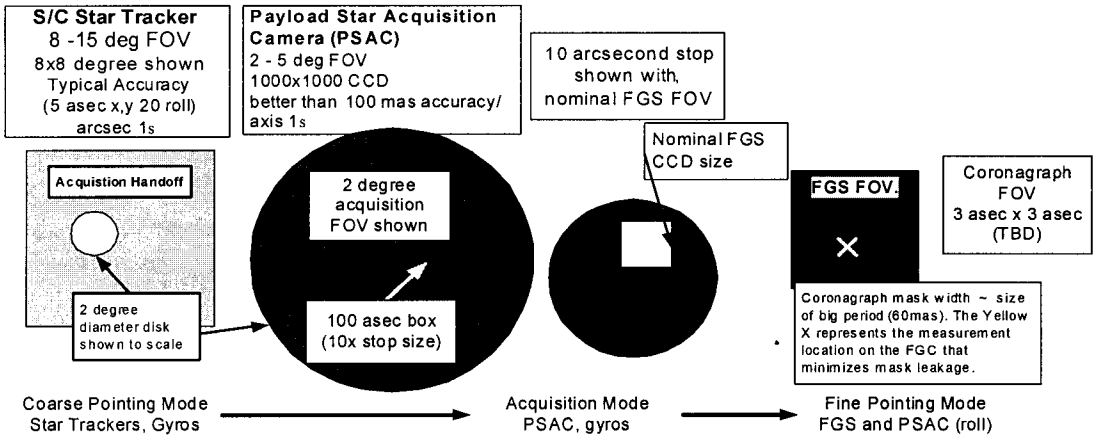

Figure 2 Acquisition scenarios

3.0 POINTING HARDWARE DESCRIPTIONS

Implementation of the pointing control loops requires various actuator and sensor hardware, mounted either on the spacecraft or payload support module. This section provides representative actuator and sensor descriptions for TPF-C.

3.1 Pointing actuators

Reaction wheels

The spacecraft houses the reaction wheel assembly (RWA) and its isolation system. The FB1 design employs six reaction wheels for spacecraft attitude control and for redundancy. The FB1 design calls out a torque capability of 0.3 N-m and momentum capability of 50 Nms. The spin axes for the 6 wheels are 30 deg from the spacecraft Z (or vertical) axis and clocked 60 degrees apart around the Z axis (see Figure 3).

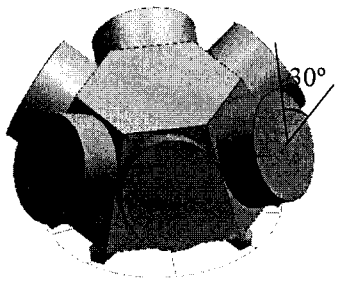

Figure 3 Reaction wheel assembly

Reaction wheels are one of the major disturbance sources in the observatory. Wheels introduce disturbance forces and torques due to center of mass offset from the rotation axis (static imbalance), angular misalignment between the wheel principal moments of inertia and the spin axis (dynamic imbalance), and bearing imperfections (harmonics). Wheels also introduce torque noise, drag torque effects, and torque ripple, which cause the torque applied to the spacecraft to deviate from the commanded torque. This mismatch between command and delivered torque can significantly affect the spacecraft pointing performance. The Goodrich E wheel published data are used for FB1 pointing analysis.

Six-axis hexapod secondary mirror actuator

The 0.9 m by 0.4 m SM is actuated by a hexapod that provides 3-axis translational and 3-axis rotational positioning. The FB1 hexapod has two stages: a coarse stage for mirror static alignment, and a fine stage to provide thermal disturbance rejection. In additional to thermal control, the hexapod can also provide tip/tilt pointing of the SM in order to correct for payload rigid body pointing errors. Piezoelectric actuation is used for both the coarse and fine stages.

As the hexapod actuates the SM assembly located at the top of the secondary tower, its reactive force/torque introduces disturbances to the payload module and excites the tower structure modes. See the deployed optical telescope assembly in Figure 4. To minimize this effect, a re-actuated design that partially cancels the reactive force/torque has been considered. The performance of the re-actuated SM design is discussed in ref. 2. Current analysis has shown that the stroke requirement required for the fine hexapod stage is around 200 nm.

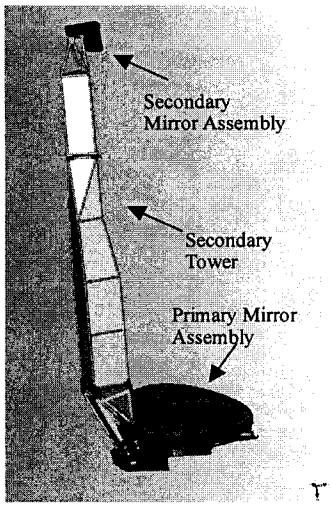

Figure 4 Optical telescope assembly (FB 1) (C. Englar)

Tip/tilt mirror

The FGM is a 13 cm flat mirror mounted on a two-axis, tip/tilt actuator stage. The piezoelectric tip/tilt actuator provides small but more rapid motion to correct for image motion error detected by the FGS. The FGM is much lighter than the SM, and the reactive disturbances on the system will be significantly smaller. However, they are introduced in closer proximity to the other optical elements, within the optical payload. Therefore, a re-actuated FGM is under consideration. The stroke required for the FGM is estimated to be around 100 asec.

3.2 Pointing sensors

Star tracker

Star trackers are employed to provide 3-axis, inertial attitude reference for the spacecraft. The FB1 design uses two trackers for redundancy, with an accuracy of 5 asec (1σ) around axes perpendicular to the tracker boresight and 20 asec (1σ) around the tracker boresight. The tracker should have a FOV of at least 8 degree by 8 degree and an update rate of no less than 5 Hz. If the tracker is capable of tracking rates up to 0.1 deg/sec, it can also be used during the large slew attitude maneuvers.

Gyros

Gyros (or an inertial reference unit) measure spacecraft body rates and are used in conjunction with star trackers for spacecraft attitude determination. High performance gyros such as the Spaced-Qualified Kearfott Inertial Reference units (SKIRU) provide accurate attitude knowledge with angle and rate random walk around 0.019 asec/sec$^{0.5}$ (1σ) and 1.33e-5 asec/sec$^{1.5}$ (1σ), respectively.

3.3 Custom sensor design

Two sets of absolute measurement cameras are placed on the coronagraph payload; the first are the Payload Star Acquisition Cameras (PSAC) which are high precision, all sky, narrow FOV star cameras mounted on the Payload Module (see Figure 5), with somewhat better noise performance than the SIRTF/Chandra class of trackers. The second is the Fine Guidance Sensor (FGS), which uses light from the coronagraph star to provide image stabilization with a fine guidance mirror (FGM), and requires a sufficiently bright star be placed by the spacecraft on a 3 asec FOV.

The PSACs will operate in "pairs" to act as a single tracking unit (two cameras mounted to the same optical bench), and will track stars down to roughly magnitude 9 to 10 by the choice of a 10 cm diameter effective aperture size. Each camera is required to provide 100 mas noise performance. The pair has a FOV separation angle of 30 degrees, and will be able to provide high precision 3-axis attitude information, with the roll accuracy only about two times worst than the other axes. The optical throughput should be roughly 50% from photons at the aperture to electrons. Depending on the spectral type of star, the PSAC should measure 8 to 40,000 electrons per visual magnitude = 9 star per 5 Hz. At the galactic poles there are roughly 1.3 stars/deg^2 brighter than magnitude 9, and 3.5 brighter than magnitude 10. Based on a pixel size of 4 to 9 asec (2 to 5 deg FOV, 2048^2 detector), a measurement noise of approximately 100 mas *Noise Equivalent Angle* (NEA)/frame for each magnitude 9 star can be attained. Using multiple stars, the NEA per tracker could be as low as 25 mas NEA at the galactic poles, and overall NEA of 50 mas in the third axis. The accuracy of the PSAC relative its mounting surface should be better than 300 mas (3σ) all axes.

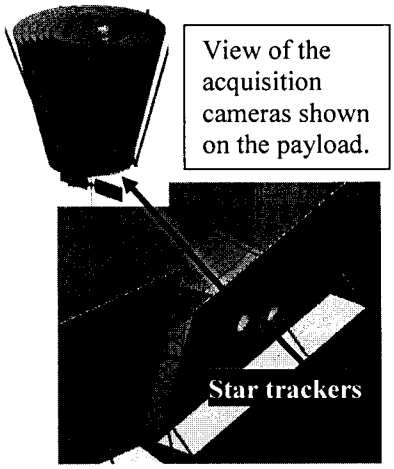

Figure 5 Payload star acquisition camera location

The PSACs will be used both to support the handoff from S/C pointing to the FGS, and to provide roll about the line of sight to the coronagraph and the general astronomical instrument (GAI). For coarse pointing of the GAI, the PSAC can provide attitude knowledge on the order of 100 mas at 5Hz.

The FGS is a combination of a FGM and a tracking sensor. The FGM controls star location on the coronagraph mask, with the goal of preventing the central star light from leaking past the mask, with a requirement of 0.3 mas offset to minimize the light leakage. The coronagraph target star light is collected by the 22 square meter primary mirror. The FGC will make use of some of the rejected light. The sketch (Figure 6) shows how the light goes through the primary-secondary mirror combination, is steered by an FSM to the coronagraph, where the light is then reflected off the

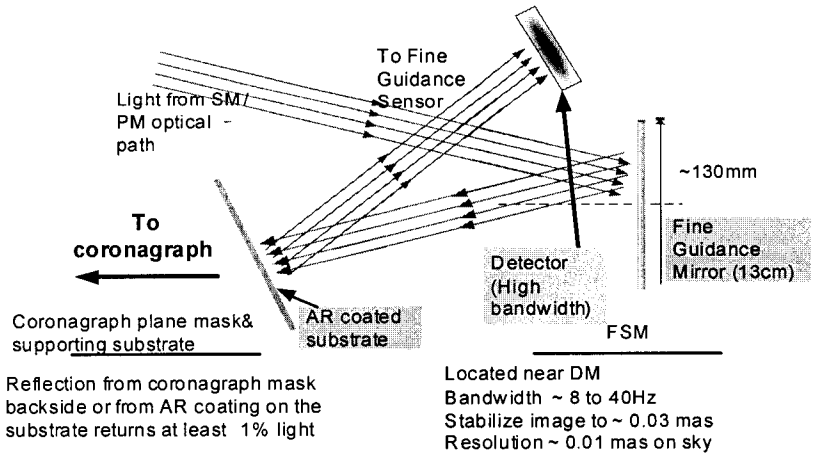

Figure 6 Fine guidance system design

surface of the substrate holding the mask, and returned to a detector for measurement of a star centroid. Roughly 20% of the light entering the telescope will arrive at the coronagraph mask due to splitting the beam for polarization and choice of bandpass filter. Since the primary mirror is 8m x 3.5m, even with a 99% loss on the coronagraph surface, the remaining light will still produce more than 10^7 electrons/second for a magnitude 7 star. The diffraction limited PSF has a $\lambda_{0.6}/D_{8m}$ = 15.5 mas in the long 8 m axis, (35.3 mas in the short axis), with a PSF width roughly 35 mas (80 mas short axis). The mask jitter budget due to beamwalk is 0.04 mas, or 1/900 of the PSF, requiring about 810,000e at the bandwidth of the system, or about 24 Hz. For the GAI, where the requirement is 3 mas – 100 times looser – the required star on the coronagraph can be much dimmer. Since the noise grows with the square root of the signal for photon noise dominated systems, the requirement is about 1/12 the PSF, which should be achievable with less than 10,000e, allowing stars as dim as 17th magnitude at the same bandwidth.

4.0 POINTING CONTROL MODES

From the acquisition layout discussed in Section 2.3, three pointing control modes were developed for FB1 design. Descriptions and functionalities of each control mode are discussed in this section, and representative mode performance will be shown in the next section.

4.1 Coarse Mode

The coarse mode includes observatory slew and coarse pointing. During coarse pointing, the ACS uses reaction wheels to maintain observatory attitude stability and employs a Kalman filter to optimally combine gyro and star tracker information for attitude estimation. The control algorithm for coarse pointing uses a proportional-integral-derivative (PID) controller and a third-order elliptical structure filter to suppress flexible mode responses. The outputs from the PID and structure filters form the three-axis acceleration commands which are multiplied by an estimate of the observatory inertial matrix to generate the torque commands. This procedure effectively decouples control among the spacecraft axes. The open- and closed-loop transfer functions from torque input to attitude output are shown in Figure 7. The open-loop system has single-axis gain and phase margin of 9.4 dB and 34.8 deg, respectively. The loop is sampled at 5 Hz with closed-loop control bandwidth of about 0.043 Hz. A simple functional diagram of the coarse mode is shown in Figure 8.

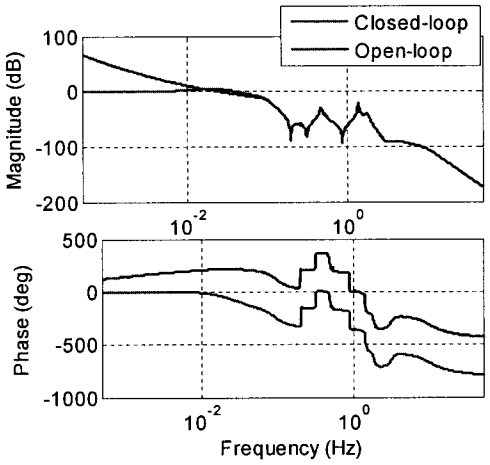

Figure 7 ACS closed- and open- transfer functions

During the mission lifetime, TPF-C is expected to perform several 30-degree, large dither maneuvers about the spacecraft Z-axis and other slews for re-targeting. Since slew rates for these maneuvers are expected to be small, the gyro/tracker combination can again be used to provide coarse attitude estimates. During the slew operation, the control algorithm is slightly modified from coarse pointing – the integrator term is eliminated to avoid accumulating large attitude errors, and an acceleration feedforward term is added to the algorithm for tracking purposes[5]. In addition, the slew profile is carefully chosen to ensure smooth (continuously differentiable) attitude, rate, and acceleration trajectories and to avoid reaching wheel torque or momentum limits during slew[5]. Such a profile would minimize flexible mode excitation and reduce the amount of settling time required after completing the slew.

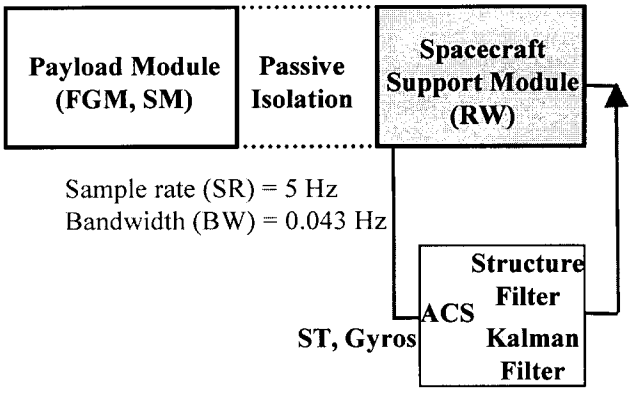

Figure 8 Coarse mode functional diagram

4.2 Acquisition mode

Once the slew maneuver is completed, coarse pointing control brings the target into the payload PSAC FOV. Then the acquisition phase begins to bring the target to the fine guidance sensor FOV. The control architecture for this mode is nearly identical to the coarse pointing mode, except the spacecraft attitude is measured from the PSAC with body rates derived from the attitude signals. As a result, the stability margins and closed-loop bandwidth of this mode are the same as the coarse pointing mode. With a better sensor, this mode is expected to achieve better pointing stability than the coarse mode. See Figure 9 for acquisition mode function diagram.

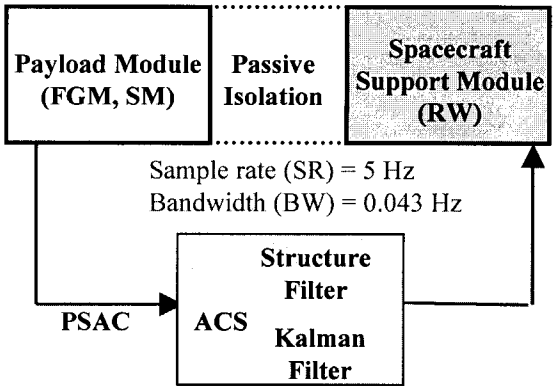

Figure 9 Acquisition mode functional diagram

4.3 Fine pointing mode

When the FGS acquires the target, the system enters fine pointing mode and activates a three-stage, pointing control system to suppress the image motion jitter and rigid body pointing errors. The FB1 passive system concept employs the ACS for low-frequency payload pointing, the secondary mirror control (SMC) for reducing low-to-mid frequency errors, the image motion control (IMC) system for compensating mid-to-high frequency errors, and the passive isolation system for decreasing any errors outside of the controller bandwidth. To implement this concept, the IMC actuator motion is sent to the SMC as a method to offload the pointing demand on the IMC, and similarly, the SMC actuator motion is sent to the ACS to de-saturate the SMC. Functional diagram of this mode is shown in Figure 10.

In the fine pointing mode, the ACS provides the first stage pointing; it uses the same low-bandwidth PID controller and structure filter as coarse and acquisition modes. The sample rate and closed-loop bandwidth of the ACS remain at 5 Hz and 0.043 Hz, respectively. The feedback signals for X and Y-axes rotations are secondary mirror (SM) angular motions, while the Z-axis pointing information comes from the PSAC. Since the SM angular motions can be measured at better accuracy than the PSAC, the pointing performance around X and Y-axes are expected to be better than the acquisition mode even with just the ACS loops closed.

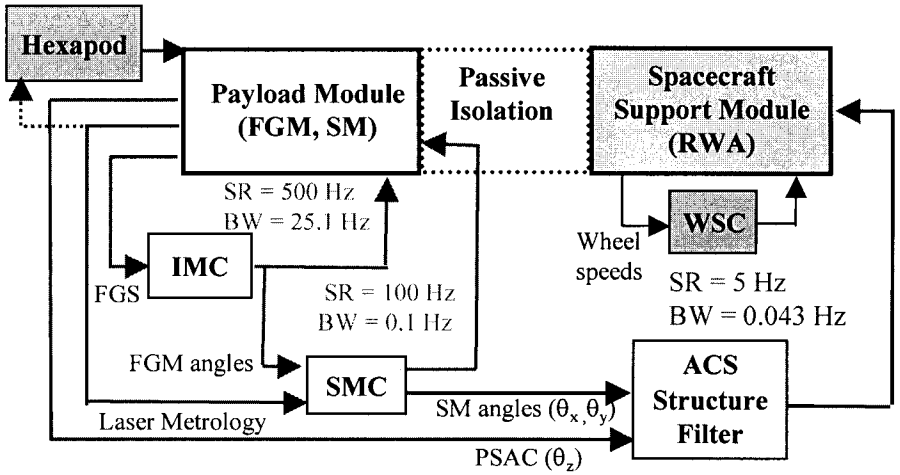

Figure 10 Fine pointing mode functional diagram

The SMC is responsible for second stage X-Y pointing, aiming to correct for pointing errors that cannot be reduced by the ACS. More specifically there are residual payload pointing errors after closing the ACS loops which can introduce excessive beamwalk on all the optics and violate the beamwalk contrast requirement discussed in Section 2.2. In this case, the SMC uses the 6-axis hexapod mechanism to orient the SM, re-centers the beam onto the nominal optical axis, and minimizes beamwalk on optics downstream of the SM. The feedback signals for the SMC come from the fine guidance mirror rotations as part of the staged control concept. The FB1 control algorithm for the SMC includes a second order low pass filter and a lead compensator with 45° maximum phase shift occurring at 0.1 Hz:

$$G_{SMC} = K_s \left(\frac{\omega_s^2}{s^2 + 2\zeta_s \omega_s s + \omega_s^2} \right) \left(\frac{1}{\beta_s} \frac{s + 1/T_s}{s + 1/\beta_s T_s} \right) \tag{1}$$

where $K_S = 10^4$, $\omega_S = 6.28 \times 10^{-3}$ rad/sec, $\varsigma_S = 0.7$, $\beta_S = 0.172$, and $T_S = 3.842$. The closed-loop response of the SMC functions is similar to a high-pass filter as shown in Figure 11 (solid line). It offers disturbance rejection at low frequencies until about 0.1 Hz.

Besides pointing, the SMC is also capable of controlling all six degrees-of-freedom of the SM and will be used to reduce the relative position and rotation errors between the primary mirror (PM) and the SM. The relative PM-SM errors are measured by the payload metrology system and sent to the SMC for hexapod control. The design and performance specs of the metrology system are subjects of another paper[6]. The sampling rate of the laser metrology system is likely to be on the order of 1 KHz; however, the SMC has low control bandwidth (~0.1 Hz) and can tolerate much smaller sampling rate. The exact sample rate for this loop will depend on the data rate availability of the FGM angular motions.

The final X-Y pointing stage is performed by the IMC system, where the two-axis FGM corrects for error signals from the FGS as discussed in Section 3.3. Error signals from the FGS are sampled at a rate of 500 Hz to enable a ~25 Hz control bandwidth on the FGM. The FB1 IMC algorithm features the same filter design as the SMC:

$$G_{IMC} = K_f \left(\frac{\omega_f^2}{s^2 + 2\varsigma_f \omega_f s + \omega_f^2} \right) \left(\frac{1}{\beta_f} \frac{s + 1/T_f}{s + 1/\beta_f T_f} \right) \quad (2)$$

where $K_f = 900$, $\omega_f = 6.28$ rad/sec, $\varsigma_f = 0.7$, $\beta_f = 0.172$, *and* $T_f = 0.013$. The lead filter has a maximum phase change of 45° at 30 Hz. The closed-loop response of the IMC is shown as a dashed line in Figure 11. It provides about 60 dB reduction for input disturbance lower than 1 Hz, and the amount of reduction gets worse until the IMC bandwidth around 25 Hz.

Although the IMC appears to have larger rejection capability than the SMC in terms of magnitude and frequency, its performance is constrained by the amount of available stroke. The intention of the control design is to use the SMC for rejecting larger, lower frequency disturbances while the IMC corrects for smaller but fast changing disturbances.

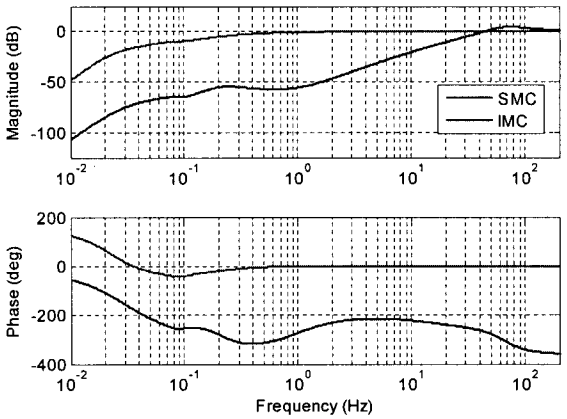

Figure 11 Closed-loop response of secondary mirror control and image motion control

5.0 DITHER/SLEW SIMULATION

The current observation scenario demands 30 deg rolls, also referred to as "dithers", around the LOS (body Z) axis. This technique forms two nearly identical speckle patterns that can be differenced to eliminate background noise and reveal a planet near the star. The objectives of this section include presenting a dynamic model used for slew/settling time simulations and illustrating some performance results.

5.1 Dynamic simulation model

A detailed integrated linear model that includes structure, optics, control, and disturbance sub-discipline models has been assembled for frequency based disturbance and noise analysis. The results of those analyses are presented in the companion paper[1]. A separate dynamic model has been developed from the JWST Yardstick model[5] to include nonlinear attitude dynamics, and actuator and sensor nonlinearities. The objective of the time-domain simulation model is to obtain representative slew performance and estimate the amount of settling time required to re-enter the fine pointing mode after completing a large slew.

Many aspects of the time simulation model are similar or identical to the linear model. The simulation dynamics include rigid body attitude dynamics and a reduced set of 35 flexible modes that are significant to image motion observed at the detector. The various control algorithms (ACS, SMC, IMC) discussed in Section 4 are implemented both in the linear and nonlinear time-domain simulation models. The optics models are implemented using sensitivity matrices that map the physical motions of each optic to image jitter measured at the detector or the amount of beam walk seen on each optic.

There are several sources of disturbances acting on the observatory. The solar radiation pressure torques introduce external disturbances on the system and are considered constant during the simulation period. Reaction wheels as discussed in Section 3.1 create internal disturbance forces and torques due to wheel imbalance and bearing imperfections, as well as nonlinear effects such as drag (friction) torque, torque quantization, and torque ripple. Sensor noises after filtering by the closed-loop dynamics also generate perturbations to pointing and image motion. All the sensor components presented in Section 3.2 and 3.3 have noise specs which are implemented as band-limited white noise in the simulation. The simulation includes currently known actuator disturbances and sensor noises, but only the nonlinearity effects on the system and the slew/settle performance are closely examined in this paper.

5.2 Wheel drag and tachometer noise effects

Reaction wheel drag torque

Reaction wheel drag torque (friction) is one of the dominant nonlinear effects identified for the PCS. The amount of wheel drag acting against the commanded torque is associated with lubrication properties and integrity of ball bearings[7]. The drag profile can change with time due to material or temperature changes. Figure 12 shows a representative wheel drag model which is not a linear function of the wheel speed (or momentum). For most missions, the wheel drag is usually compensated by the integral control in the ACS algorithm if the change in drag remains small and slowly varying during science observation. However, TPF-C has stringent pointing stability requirements and may not tolerate even small changes in wheel torque variability.

To test how wheel drag affects pointing performance, the drag profile shown in Figure 12 is implemented in the time simulation model. The rigid body pointing stability for the case without wheel drag is illustrated as a solid line in Figure 13(a), whereas the case with wheel drag is plotted as a dashed line. Clearly when wheel drag is present, it takes the integral control a long time to reduce the pointing error. The long transient time is partly due to the large time constant associated with the ACS integral control (~700 sec), but if the disturbance (drag in this case) changes constantly, the integral control may never "catch" up to compensate for the disturbance. Only pointing error around the X-axis is shown here since the pointing around the other two axes demonstrate similar error trends.

A simple solution for rejecting the wheel drag torque is to implement a local wheel speed feedback loop that has much higher bandwidth than the ACS controller. The FB 1 wheel speed control (WSC) loop consists of an integrator and a lead compensator with 60 deg phase change at 1 Hz:

$$G_{WSC} = \left(\frac{K_w}{s}\right)\left(\frac{s+z_1}{s+p_1}\right) \tag{3}$$

where $K_w = 18.27$, $z_1 = 1.68$, and $p_1 = 23.45$. The closed-loop bandwidth for WSC is about 1 Hz which is more than 20 times larger than the ACS bandwidth. The performance of the WSC coupled with the fine pointing control systems

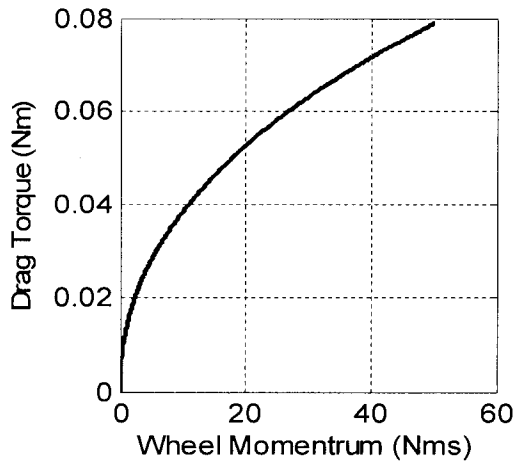

Figure 12 Representative wheel drag model

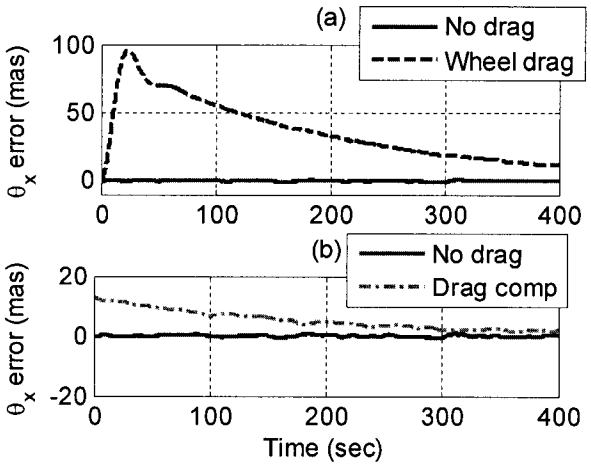

Figure 13 Simulation results: (a) wheel drag (b) wheel drag plus drag compensation

is illustrated in Figure 13(b). According to the simulation results, the closed-loop system is now capable of achieving desired rigid body pointing performance by rejecting changing wheel drag torques.

Reaction wheel tachometer measurement noise

Closing the wheel speed loop greatly reduces the wheel drag effects, but it also introduces noises into the system due to tachometer (tach) measurement errors. The simulation results shown above do not contain any tach errors; these effects are considered here. Through the WSC system, the tach errors become part of the wheel torque commands, which in turn propagate through the plant dynamics and affect pointing stability. The magnitude of the wheel speed measurement error depends on the tachometer design. For FB 1 design, a digital tach is employed, where a fast onboard clock measures the time elapsed between pulses located at known locations of the wheel. For example, the Goodrich E wheel has 72 pulses/rev, or equivalently, one pulse for every 5 degrees of rotation. An estimated wheel speed is obtained by dividing the pulse angle by the time measurement. There is one caveat associated with this simple design – as the wheel speed increases, the amount of time elapsed between two pulses decreases and the resulting speed estimation error increases. The tach error bound versus wheel speed for an E wheel is shown in Figure 14 (solid line) which indicates that the tach error may be as much as 5 revolution-per-minute (RPM) at high wheel speeds. Tach error can easily be reduced by increasing the number of pulses/rev or increasing the number of pulses for time measurement.
Figure 14 illustrates that the tach error bound decreases as the number of pulses per revolution decreases. The dashed and dotted lines in this figure correspond to tachometer with 18 and 6 pulses/rev, respectively. However, this approach limits the smallest wheel speed that can be measured given the loop sample time (Δt) and pulses/rev (α):

$$\omega_s \geq \frac{1}{\Delta t}\frac{1}{\alpha} \quad \left[\text{rev}/\text{sec}\right]. \tag{4}$$

For the problem at hand, it is desirable to bias the wheel speed above 3 RPS to avoid zero-speed crossing and exciting low frequency modes[2]. It is also beneficial to implement fewer pulse/rev to reduce the magnitude of the tach error. Setting $\omega_s = 3$ RPS and $\alpha = 6$ pulses/rev, Equation 4 is used to determine the required minimum sample time of Δt = 0.056 sec or maximum sample rate of 18 Hz. The resulting sample rate should be at least ten times greater than the WSC closed-loop bandwidth. In this case, an 18 Hz loop sample rate is sufficient in accommodating the WSC with a closed-loop bandwidth of 1 Hz. Implementing the tachometer measurement error in the time simulation, the rigid body pointing error around X-axis is shown in Figure 15(a), while image motion error around the same axis is illustrated in Figure 15(b). The pointing error around the Y-axis is not shown, since it is similar to the X-axis performance. With the assumed tach design (6 pulses/rev and time measured between two pulses), the rigid body pointing requirement (12 mas, 3σ) can be satisfied for wheel speeds less than about 2500 RPM. On the other hand, the LOS image jitter requirement (0.9 mas, 3σ) is met for all wheel speeds, since the SMC and IMC are capable of suppressing tach noise effects on image jitter.

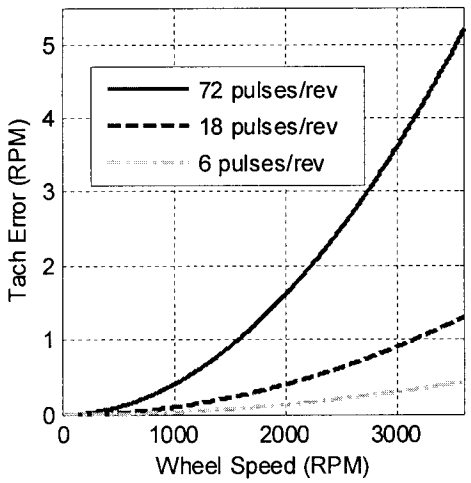

Figure 14 Tach error bound versus wheel speed

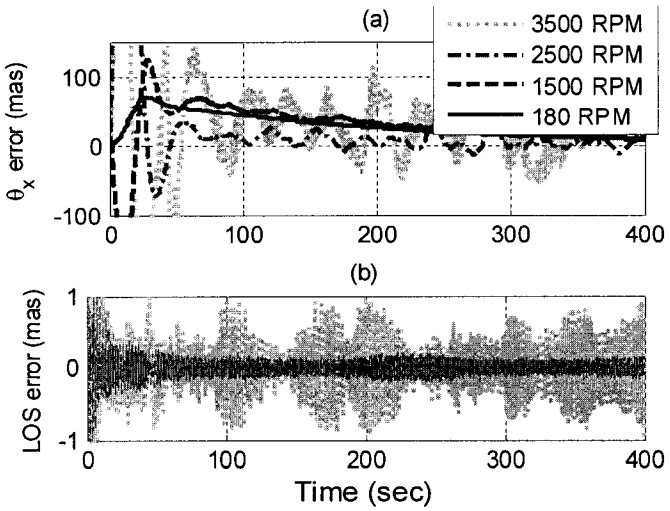

Figure 15 (a) Rigid body X-axis pointing performnace (b) LOS X error for various tach error levels

5.3 Representative slew/settle performance

To demonstrate slew/settle performance, the spacecraft is commanded to maintain its attitude for the first 100 sec, rotate around the LOS (or body Z axis) for 30 degrees, and stay at the new orientation until the vibrations settle. Figure 16 shows the rigid body pointing angles during the slew/settle simulation. The top two plots are θ_x and θ_y angular errors with the solid horizontal lines indicating their 3σ pointing requirements. The bottom plot illustrates the smooth 30-deg roll about the LOS (or body Z axis). For this simulation, the slew maneuver takes about 520 sec, occurring between 100 and 620 sec. Then the acquisition phase begins at 620 sec and ends at about 855 sec when the rigid body pointing requirements are met. The wheel speeds at the end of the maneuver range between 200 and 500 RPM. Tach error does not significantly affect rigid body pointing stability during this manuever.

At the end of acquisition mode, the target is in the FGS FOV where the IMC and SMC can be activated to stabilize the image motion. Figure 17 illustrates the LOS X and LOS Y motions during the fine pointing phase, and again the solid horizontal lines show the 3σ image motion requirements (9 mas, 3σ). The LOS jitter is dominated by a low frequency (~0.26 Hz) and low damping (0.1%) mode. After some investigation, this mode is mainly excited by the tach error, and therefore, similar behaviors are also observed in Figure 15(b).

The current operation efficiency requirement on slew/settle is about 30 min (1800 sec) for a 30-deg slew. The total time required for slew/settle maneuver is defined by the amount of time required for slew plus the time required for rigid body pointing (θ_x and θ_y) and LOS jitter to meet their fine pointing requirements. Figure 16 and 17 demonstrate that the total slew/settle time is about 855 sec for a representative maneuver which easily satisfies the 1800 sec time requirement. It should be noted that slew/settle results would vary with initial conditions. More analysis is required to identify the worst-case slew/settle time.

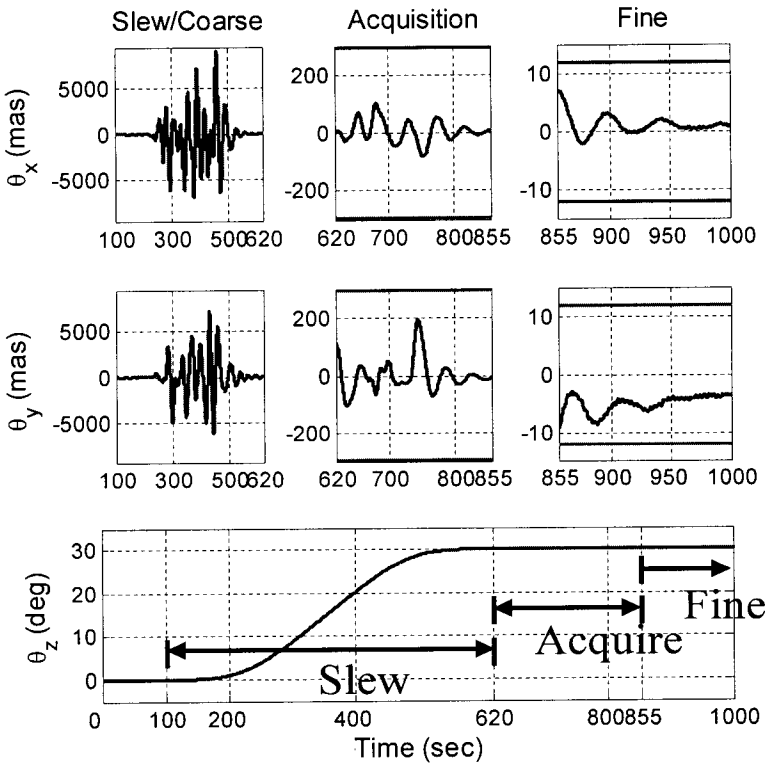

Figure 16 Rigid body pointing angles for slew/settle simulation

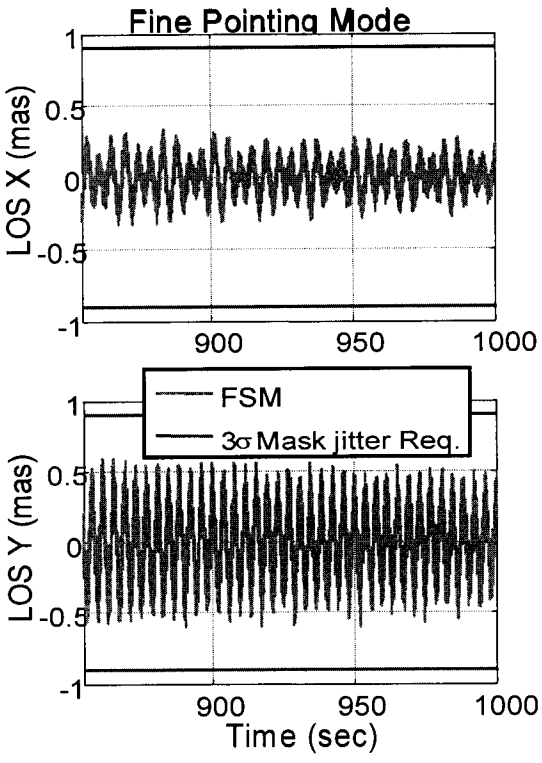

Figure 17 LOS errors for slew/settle simulation

6.0 SUMMARY AND FUTURE WORK

This paper provides an overview of the pointing control system for TPF-C flight baseline 1 design. Brief descriptions of the off-the-shelf pointing hardware components, along with custom sensor designs, are presented to demonstrate that the TPF-C passive pointing design relies mainly on heritage technologies. Control architectures, as well as control algorithms, for three pointing modes (coarse/slew, acquisition, and fine) are discussed in detail. Integrated dynamic simulation models have been developed to verify the performance of the pointing system for each mode. Preliminary results demonstrate that adding a reaction wheel speed feedback loop can reject wheel drag torque. If the tach noise introduced from the speed feedback loop is too large, the rigid body pointing performance may not meet requirements. However, better tach designs that reduce the tach noise compared to the current concept can be implemented to resolve this problem. Finally, representative slew/settle simulations demonstrate that operation efficiency or time requirements can be met using the current pointing design.

A number of activities have been planned to enhance the current design and analysis:

- Incorporate the active pointing and isolation system in time simulation model
- Consider other control designs and perform more rigorous robustness analysis on the multi-loop design
- Update the time simulation model to include more accurate actuator and sensor models
- Explore other tachometer design options to reduce wheel speed measurement errors
- Refine fine guidance system design to determine the location of focal plane and specify hardware capabilities

ACKNOWLEDGEMENT

The authors would like to thank Andy Kissil at JPL and Sandra Irish at GSFC for support with the structural modeling, Philip Dumont at JPL for assistance with the optical modeling, and Stuart Shaklin at JPL with support for the error budgeting. We also appreciate guidance and helpful feedback from Marie Levine (integrated modeling lead) and Virginia Ford (design team lead).

REFERENCES

1. V. G. Ford, "Terrestrial Planet Finder Coronagraph 2005: overview of system design studies and technology development", SPIE Optics and Photonics, San Diego, 2005
2. C. Blaurock, K.-C. Liu, L. Dewell, J. Alexander, "Passive isolator design for jitter reduction in the Terrestrial Planet Finder Coronagraph", SPIE Optics and Photonics, San Diego, 2005
3. L. Dewell, C. Blaurock, K.-C. Liu, J. Alexander, "Precision telescope pointing and vibration isolation for the Terrestrial Planet Finder Coronagraph", SPIE Optics and Photonics, San Diego, 2005.
4. S. B. Shaklin, L. F. Marchen, J. J. Green, "The Terrestrial Planet Finder Coronagraph error budget", SPIE Optics and Photonics, San Diego, 2005.
5. Mosier, G., Femiano, M., Ha, K., Bely, P., Burg, R., Redding, D., Kissil, A., Rakoczy, J. and Craig, L., "Fine Pointing Control for a Next Generation Space Telescope," SPIE Vol. 3356, Space Telescopes and Instruments V, 1998.
6. Stuart B. Shaklan, Luis F. Marchen, Feng Zhao, Robert D. Peters, Timothy Ho, and Buck Holmes, "Metrology system for the Terrestrial Planet Finder Coronagraph," Proc. SPIE Int. Soc. Opt. Eng., 2004.
7. Bill Bialke, "A Compilation of Reaction Wheel Induced Spacecraft Disturbances," 20th AAS Guidance and Control Conference, 1997.